Metals and Materials International (2024) 30:1321–1330
https://doi.org/10.1007/s12540-023-01575-8

Mechanical Stability of Retained Austenite and Texture Evolution in Additively Manufactured Stainless Steel

Hobyung Chae[1] · E-Wen Huang[2] · Jayant Jain[3] · Dong-Hyun Lee[4] · Stefanus Harjo[5] · Takuro Kawasaki[5] · Soo Yeol Lee[4]

Received: 24 August 2023 / Accepted: 6 November 2023 / Published online: 8 December 2023

Abstract
We employed two additive manufacturing (AM) strategies perpendicular to each other in AM stainless steel. In contrast to the vertically-built strategy, the horizontally-built one imposed higher tensile strength and ductility due to distinct transformation-induced plasticity (TRIP) behavior and a tailored initial texture oriented more favorably for deformation texture. We applied the direct-aging-treatment without solid-solution to retain unique AM microstructure and retained austenite (RA), which enhanced yield strength (+ 60.2%), tensile strength (+ 41.2%), and ductility (+ 81.2%). This effective strengthening by the direct-aging-treatment effectively increased the stability of RA delaying the onset of TRIP. This is because RA grains possessed relatively homogeneous chemical composition by aging and are effectively suppressed by a harder neighbored precipitated-martensitic matrix despite the increase of stacking fault probability. Our findings offer a promising paradigm for tailoring properties of texture-controlled AM steels with the aging strategy and advance a fundamental understanding of the intrinsic deformation behavior of AM metals.

Keywords Additive manufacturing · Aging-treatment · Mechanical stability · Transformation-induced plasticity · Steel

1 Introduction

To expand application of steels, retained austenite (RA) is considered as important factor, because transformation-induced plasticity (TRIP) from RA to martensite can retard a necking and contribute to an increase in strength and elongation [1, 2]. Thus, one of the key techniques for adjusting the tensile characteristics is to manage the mechanical stability of RA transformed during deformation. The RA stability intrinsically depends on its shape [3] and size [4–6] within the matrix, the concentration of interstitial atoms [7], and the texture [8, 9], and extrinsically relies on its neighboring phases [10]. Therefore, it is crucial to comprehend how inherent and external factors affect the RA stability and how these influence plastic behavior.

Precipitation-hardened (PH) martensitic stainless steel has high corrosion resistance and remarkable strength, however, lower formability [11, 12]. Due to the unique thermal history imposed by the additive manufacturing (AM) process [13], steel component can overcome its formability deficit using RA [14–16]. AM PH steel exhibits a wide range of mechanical properties [17–26]. A high fraction of RA induces a lengthened elongation but lowers yield strength [27] and deteriorates aging efficiency [28, 29], thereby, appropriate heat-treatment should be accompanied [30].

To optimize the properties of PH steel, many studies controlling scanning strategy and energy density [31, 32], AM atmosphere [33], and post-heat-treatments [34] were carried out. The control of RA amount by time intervals between layers leads to microstructural evolution using a variety of scanning strategies [35], which revealed that the nature and distribution of RA are highly influenced by the building

✉ E-Wen Huang
EwenHUANG@nctu.edu.tw

✉ Soo Yeol Lee
sylee2012@cnu.ac.kr

[1] Neutron Science Division, Korea Atomic Energy Research Institute, Daejeon 34057, Republic of Korea

[2] Department of Materials Science and Engineering, National Yang Ming Chiao Tung University, Hsinchu 30013, Taiwan

[3] Department of Materials Science and Engineering, Indian Institute of Technology, New Delhi 110016, India

[4] Department of Materials Science and Engineering, Chungnam National University, Daejeon 34134, Republic of Korea

[5] Neutron Science Section, J-PARC Center, Japan Atomic Energy Agency, Tokai-mura 319-1195, Japan

strategy. However, in contrast to the microstructural works, studies on the stability of RA and its TRIP behavior under deformation determined by different thermal histories have rarely been reported. Our earlier work [36] reported that different AM strategy induced the plastic anisotropy by difference in initial RA and texture. In addition, aging-treatment without solid-solution in AM as-built sample imposed very effective strengthening without sacrifice of ductility due to preservation of unique AM microstructure and RA [37, 38].

In this work, we examined the mechanical stability of RA, texture development, and their influence on plastic anisotropy using in-situ neutron diffraction. We manufactured the AM steels with different thermal histories, after which we had directly-aging-treatment to strengthen the as-built sample. The stability of RA in vertically and horizontally fabricated components was revealed in terms of applied stress, strain, and austenite phase strain. Then, the reasons for changes in TRIP behavior depending on the stability were discussed. In addition, the texture evolution of martensite in conjunction with TRIP was examined from the changes in integrated intensities for *hkl* reflections. This study suggests not only the methodology to observe the stability of RA but also what influences the stability of RA. To control activation of TRIP by post-process and to optimize the quantity of RA and initial texture by AM strategies would contribute to tailoring the plasticity of AM materials.

2 Materials and Methods

2.1 Sample Preparation

Dog-bone-shaped tensile samples with gauge length of 10 mm and diameter of 6 mm were additively manufactured using 15-5PH metallic powder and the direct-metal-laser-sintering method (Fig. 1). Those samples were composed of 14.8 wt% Cr, 4.5 wt% Ni, 3.2 wt% Cu, 0.07 wt% C, and Fe balance. Vertical and horizontal types of the samples were considered, where the axial axes of V-AB and H-AB were parallel and perpendicular to building direction (Fig. 2a and b). Since both samples were deposited directly into cylinder-shaped tensile specimens, this building strategy induced a smaller and wider deposited area for V-AB and H-AB, respectively, and thus different thermal histories were derived by different interval times, Δt, between layers ($\Delta t_v < \Delta t_h$). Detailed AM conditions are as follows: a power (~ 195 W), a spot size (~ 70 µm), a hatch spacing (~ 0.1 mm), a layer thickness (~ 40 µm), scanning strategy (orthogonal), a scanning speed (~ 1200 mm/s), atmosphere (nitrogen) were used. A directly-aging-treatment (modified H900 heat-treatment) leading to effective strengthening by bearing Cu-precipitates from the as-built samples indicates that the as-built sample was heat-treated at 482 ℃ for 1 h followed by air cooling. Microstructure information can be found in Table 1, Fig. S1, and our earlier works [36–38]. We denoted vertically and horizontally as-built samples as V-AB and H-AB, and directly-aged samples as V-A and H-A.

2.2 In-situ Neutron Diffraction

The in-situ time-of-flight (TOF) neutron diffraction experiments were conducted using TAKUMI diffractometer at J-PARC. The TOF diffraction geometry was presented in Fig. 2c. The tensile samples were loaded and inclined 45° with respect to the incident neutron beam with 0.7–3.2 Å in wavelengths. Incident beam was diffracted with *hkl* reflections in a sample during a tensile test and diffracted beam from reflections with $Q_{\parallel}$ (loading direction//scattering vector) and $Q_{\perp}$(loading direction⊥scattering vector) in 175 mm^3 of the scattering volume was collected at axial and transverse detectors situated at ± 90°. The uniaxial tensile test was conducted with load-control mode with ~ 1.8 N/sec at elastic regime, and then, displacement control mode with 0.01 mm/min at the plastic regime. Collected neutrons during experiments were chopped every 15 min, which corresponds to symbols on stress-strain

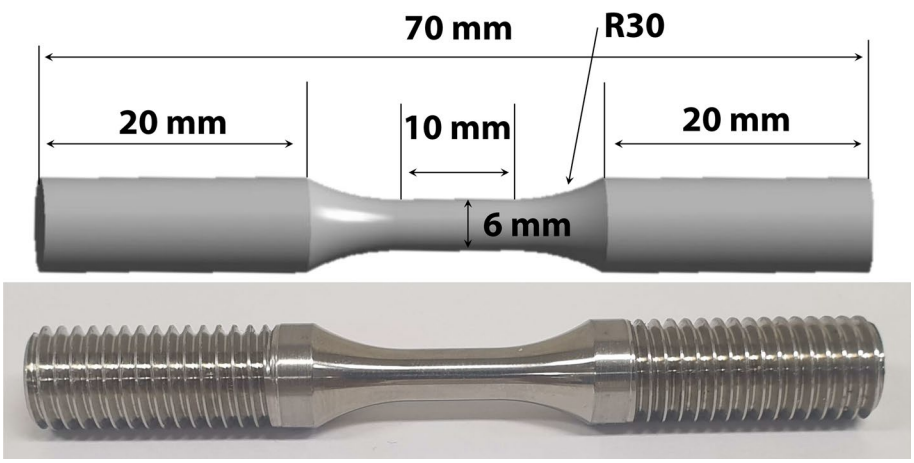

Fig. 1 The geometry of tensile sample for in-situ neutron diffraction experiment at TAKUMI engineering diffractometer

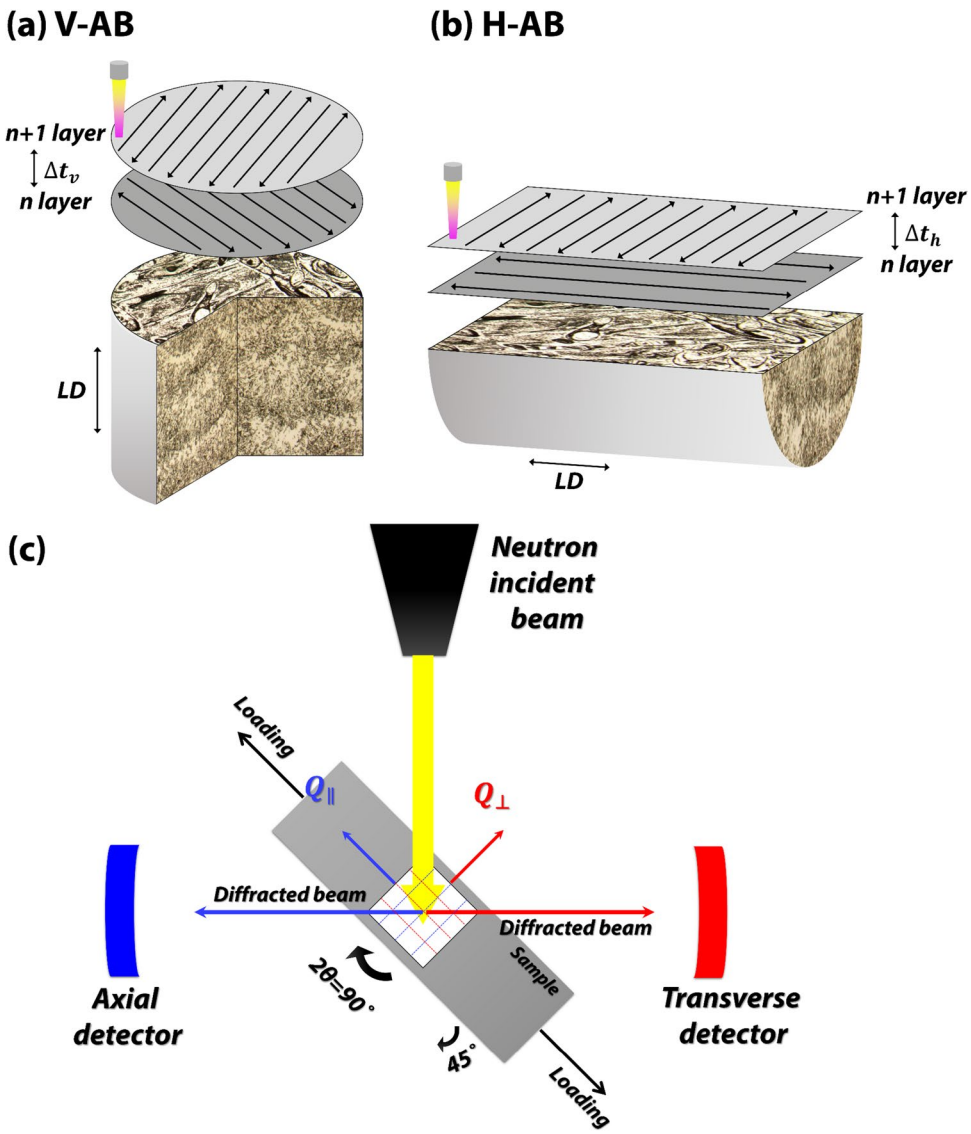

Fig. 2 **a** Vertical sample, **b** horizontal sample fabricated by additive manufacturing with different scanning strategies, **c** schematics of in-situ neutron diffraction geometry

Table 1 The effective grain size of each sample [37]

Sample	V-AB	H-AB	V-A	H-A
Size (μm)	2.8 ± 4.1	3.3 ± 4.3	2.7 ± 4.1	2.3 ± 4.0

curves in Fig. 4. The changes in lattice parameter, phase fraction, integrated peak intensity, and *hkl*s' *d*-spacing during tensile deformation were obtained from diffraction analysis. Phase strain (ϵ^{phase}) and lattice strain of *hkl*s (ϵ^{hkl}) using lattice parameter of phase constituents and *d*-spacing of *hkl* reflections obtained from Rietveld refinement and single peak fitting were calculated as follows.

$$\epsilon^{phase} = \frac{a^{phase} - a_0^{phase}}{a_0^{phase}} \tag{1}$$

$$\epsilon^{hkl} = \frac{d^{hkl} - d_0^{hkl}}{d_0^{hkl}} \tag{2}$$

where a_0^{phase} and a^{phase} are lattice parameters of constituent phase before and after loading; d_0^{hkl} and d^{hkl} are *d*-spacings of *hkl* reflections before and after loading, respectively. Relative intensity (RI^{hkl}) was employed to observe changes of integrated intensity for analyzing texture development and was calculated as follows.

$$RI^{hkl} = \frac{I^{hkl}}{I_0^{hkl}} \tag{3}$$

where I_0^{hkl} and I^{hkl} are integrated intensities before and after loading, respectively.

3 Results

3.1 Constituent Phase

Initial diffraction spectra exhibited that samples contained different RA fractions and textures (Fig. 3). V-AB revealed a RA of 7.6% and a stronger BCT{110} texture along the transverse direction (perpendicular to building direction), while H-AB possessed a RA of 14.3% and a stronger BCT{110} texture along the axial direction (perpendicular to building direction) [36, 37]. The building strategy used in this study altered the time interval between deposited layers in each sample, which resulted in a distinct thermal history. Due to a longer time interval and a larger heat sink, the horizontal sample underwent attenuated thermal cycles with lower frequency and higher temperature amplitude, as compared to the vertical sample which experienced attenuated thermal cycles with relatively higher frequency and lower temperature [39]. It might have given the horizontal sample more time to experience the austenite temperature range, which increased the fraction of retained austenite [15]. Additionally, during AM, the melt pool is solidified along a specific orientation, developing texture in the samples. Aging-treatment rarely changed the tendency of the texture and amounts of RA revealing that V-A and H-A had the RA of 6.8 and 13.7%. This is due to the temperature of the aging process that is lower than the austenite starting temperature, which only infrequently induces the driving force necessary to change austenite into martensite. It is very compatible with our earlier research (Fig. S1) [38].

3.2 Tensile Response

Aging-treatment enhanced the mechanical properties significantly compared to the as-built samples and previous works (Fig. 4) [17–26]. Note that true stress-strain curve was shown until necking (Fig. 4b). For V-AB, aging improved yield strength (YS), tensile strength (TS), and uniform elongation (UE) by 78%, 38.9%, and 50% achieving 1512, 1750 MPa, and 6.3% in true stress-strain. On the other hand, the YS, TS, and UE of H-A increased by 60.2, 41.2, and 30%, reaching 1214, 1845 MPa, and 7.8% in true stress-strain (Table 2). This improvement is attributed to Cu-precipitates evolving in the martensite by aging. We previously reported that aging treatment resulted in excellent precipitation hardening in additively manufactured 15-5PH stainless steel. This is because Cu nano-agglomerates were

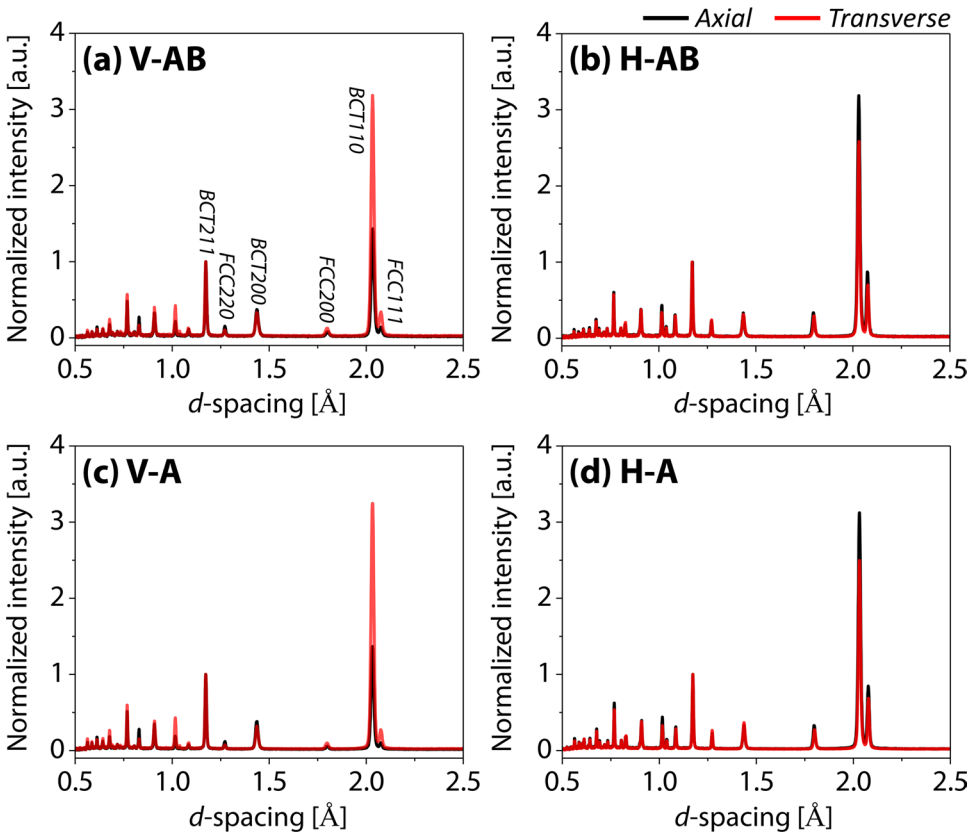

Fig. 3 Neutron diffraction spectra of **a** V-AB, **b** H-AB, **c** V-A, and **d** H-A samples, respectively, before loading (black and red lines are corresponding to axial and transverse responses)

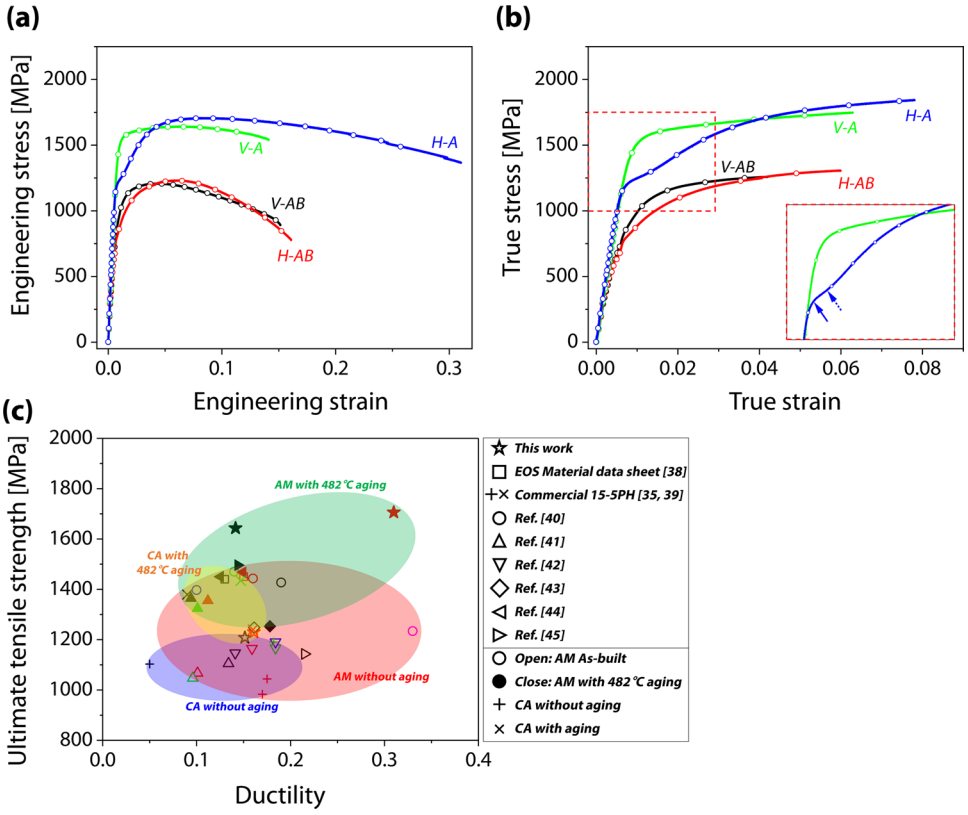

Fig. 4 **a** Engineering and **b** true stress-strain curves obtained with in-situ neutron diffraction (lines and symbols are corresponding to load-frame responses and each neutron spectrum) and its inset (magnified view of red-dash area), and **c** our work's positions compared with previous works and nominal material data sheet in engineering stress-strain values [20–26, 43, 44]

Table 2 Summary of tensile properties (in true)

Sample	0.2% offset yield strength	Tensile strength	Uniform elongation
V-AB	846	1260	0.042
H-AB	758	1307	0.060
V-A	1512	1750	0.063
H-A	1214	1845	0.078

precipitated in a martensitic matrix of unique AM microstructure with a lower Cu solubility (Fig. S2, S3, Table S1) [25, 37, 40]. Consequently, these results indicate that the aging-treatment is very effective without a strength-ductility trade-off [41, 42].

The horizontal samples showed a lower YS and an extended yielding behavior followed by an increased strain hardening during further deformation. In the H-A, this behavior is significant. The inset of Fig. 4b showed the yielding behaviors of the V-A and H-A samples in details, which correspond to the red dash box. At lower applied stress for YS of H-A, both samples demonstrated comparable bulk elasticity, however H-A displayed a lower 0.2% offset YS by 88 MPa than V-A (blue line arrow). A higher hardening rate was achieved in H-A (blow dash-line arrow). The transition of hardening rate of the horizontal samples led to a crossover with the stress-strain curve of the vertical samples, resulting in higher TS. This tendency was more obvious in aged samples, which exhibited an extended elastic-plastic transition phenomenon in the early deformation followed by more rapid strain hardening achieving outstanding TS and UE.

3.3 TRIP Behavior

The TRIP appeared differently in terms of building strategy and aging-treatment (Fig. 5a, b), as revealed in the reduction of relative RA fraction as a function of applied stress and strain. Phase transformation for V-AB and H-AB began at ~ 290 and ~ 343 MPa, while aged samples revealed little RA reduction until ~ 950 MPa, after which a sharp decrease was observed. Bars shown in the graph indicate the amount of FCC-to-BCT transformation, which can be described as a reduced RA fraction at corresponding stress and strain. V-A and H-A exhibited considerable reductions of 17.7 and 32.4% at corresponding stresses of ~ 1442 MPa and ~ 1151 MPa, while the as-built samples showed a continuous reduction throughout the deformation. The RA in all samples started to decrease before YS and was mostly consumed near TS. The vertical samples showed the earlier onset of TRIP followed by a slower reduction in RA during deformation than the horizontal samples.

The RA reduction as a function of austenite phase strain (ϵ_γ) is presented in Fig. 5c. Note that austenite phase strain

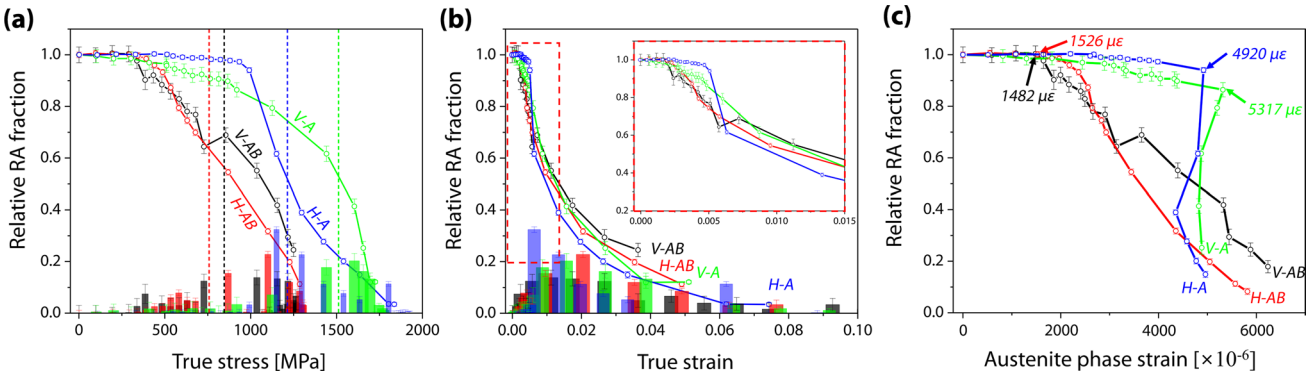

Fig. 5 Changes in relative fraction of retained austenite as a function of **a** macroscopic true stress (vertical dash lines: yield strength), **b** macroscopic true strain, and **c** austenite phase strain

is proportional to austenite phase stress. V-AB and H-AB exhibited the onset of reduction at the ϵ_γ of ~ 1482 με and ~ 1526 με, while those of V-A and H-A corresponded to ~ 5317 με and ~ 4920 με, which were much higher. While the RA in the as-built samples decreased continuously with an increase in ϵ_γ, the aged samples were independent of the accumulation of ϵ_γ.

3.4 Evolution of Diffraction Intensity

The changes in diffraction intensities and lattice strains for various *hkls* whose plane normal was parallel to the tensile axis are shown in Figs. 6 and 7. Note that lattice strain is proportional to an accommodated stress by each *hkl* reflection. The intensities of all orientations in RA (Fig. 6) decreased with increasing respective lattice strains. Martensite revealed a distinct intensity change

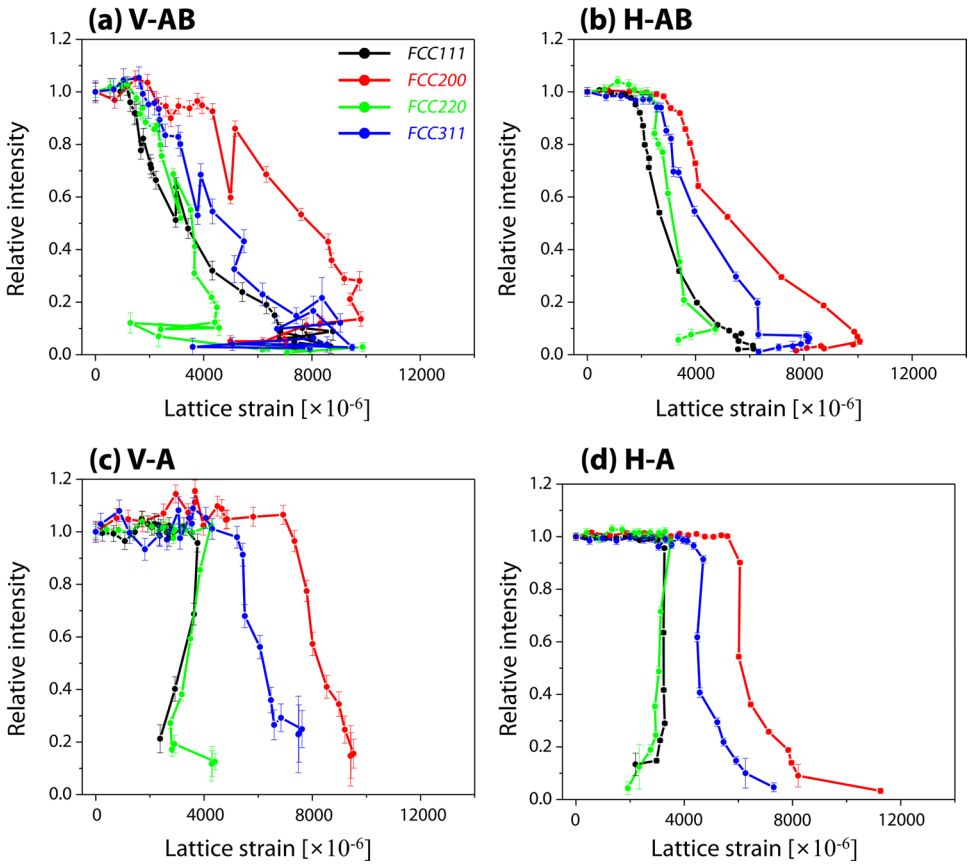

Fig. 6 Relative intensity changes in *hkl* reflections of austenite phase in **a** V-AB, **b** H-AB, **c** V-A, and **d** H-A samples (black-FCC{111}, red-FCC{200}, green-FCC{220}, blue-FCC{311})

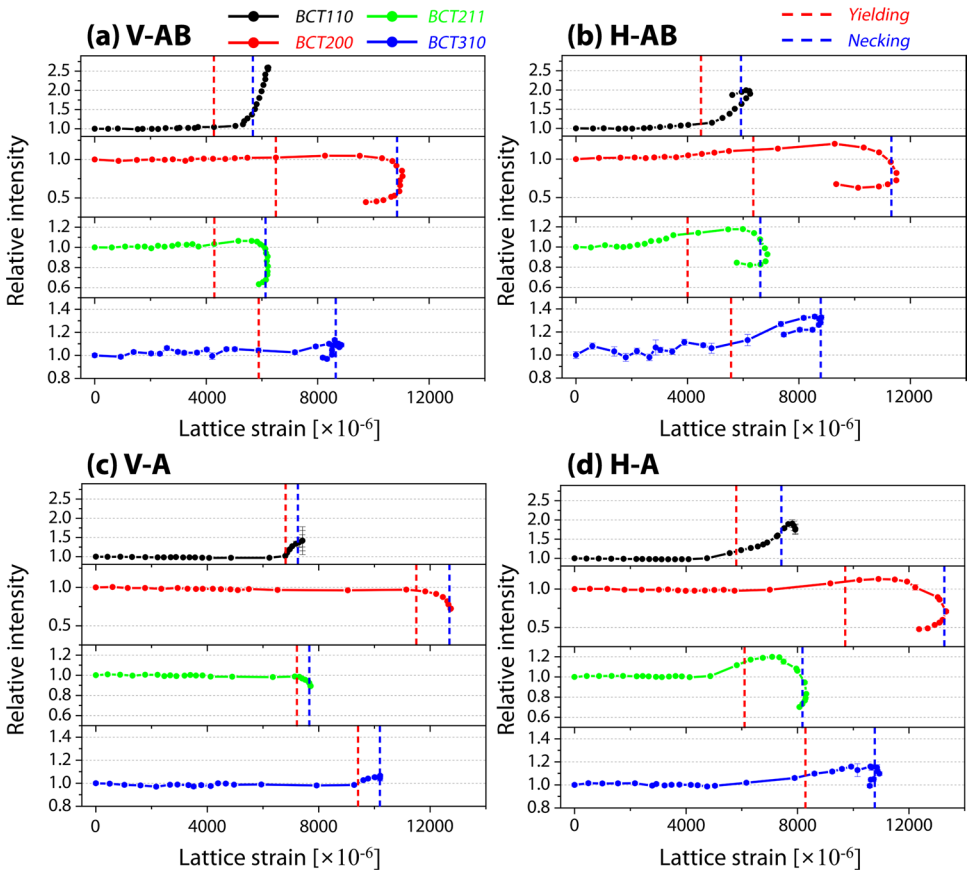

Fig. 7 Relative intensity changes in *hkl* reflections of martensitic phase in **a** V-AB, **b** H-AB, **c** V-A, and **d** H-A (black-BCT{110}, red-BCT{200}, green-BCT{211}, blue-BCT{310}. Red and blue dash line are corresponding to yielding and necking points)

under applied stress (Fig. 7). The intensities of BCT{110} and BCT{310} increased with an increase in lattice strain, while BCT{200} and BCT{211} were vice versa. The intensity evolution of the both phases was qualitatively similar to previous studies [36, 45, 46]. Global increase of intensities in all orientations of martensite was attributed to the contribution of newborn martensite by TRIP [36].

The relative intensities of BCT{110} in the axial direction began to increase near a yielding and reached a value of 1.37 in V-AB, 1.37 in V-A, 1.64 in H-AB, 1.69 in H-A at a necking. Crystal planes within each grain are unable to freely glide because the ends of the tensile bar are restrained in uniaxial tension. Constraint causes crystal planes to rotate in the direction of the tensile axis. Schmid factors are simultaneously altered during deformation, and each crystal plane in the BCC rotates towards the {110} orientation as a result [47]. Consequently, a dislocation glide, the only deformation mechanism in BCC/BCT, causes a measureable rise of {110} (or {200}) in the axial direction. BCT{110} shows a noticeable change in intensity during deformation, indicating that many slips lead to the deformation texture.

4 Discussion

The extended elastic-plastic transition shown in H-A (Fig. 4) is mainly attributed to abrupt TRIP (Fig. 5). Although these provided a significant plastic flow decreasing the YS and strain hardening rate (blue line arrow in inset of Fig. 4b), newborn martensite formed by TRIP effectively contributed to the strengthening during further strain, increasing the hardening rate (blue dash arrow in inset of Fig. 4b). It attributed to relatively higher fraction of RA in H-A. Thus, this transition near yielding in H-A should be due to the TRIP effect, as evidenced by the ~ 70% reduction in RA at the strain of 2% (Fig. 5b). This yielding was weakly observed in H-AB but consistently led to a cross-over in the stress-strain curve of vertical sample, resulting in higher TS than that of V-AB.

Aging-treatment significantly influenced the mechanical stability of RA. There existed a large difference in the onset of TRIP (critical stresses required in RA for phase transformation to BCT) (Fig. 5c). Note that ϵ_{γ} shown in Fig. 5c is linearly proportional to stresses applied to the

austenite during deformation. As shown in ϵ_γ of ~ 1500 με (for H-AB, V-AB) and of ~ 5000 με (for H-A, V-A) in Fig. 5c, the as-built samples revealed much lower onset of TRIP than the aged samples, which indicates that the as-built sample exhibited much lower stability of RA on the TRIP than the aged samples.

In as-built samples, stresses accommodated by RA increased with an increase in its TRIP resistance (Fig. 5c), which means that RA requires gradually-increased stresses to be transformed. This phenomenon can be possibly attributed to the followings: one is the inhomogeneity of the composition in RA grains and grain orientation dependency, and the other is grain refinement effect caused by a transformed martensitic area within the RA grains [5, 6], giving rise to the RA being surrounded by newborn martensite [10]. Additionally, as austenite's grain size decreases, the interfacial energy increases, requiring more driving force to transform RA and, consequently, a decrease in Ms temperature [5]. A continuous decrease in the intensities of all *hkls* of RA (Fig. 6) during plastic deformation indicates that TRIP [48] is more predominant than the development of deformation texture associated with slip activities of RA. Thus, parent austenitic grains were refined by being surrounded by newborn martensite from TRIP as well as pre-existing neighbored martensitic phase. Neighboring martensite suppressed the shear strain of RA and accommodated higher stress (stress concentration) during the applied loading conditions. Moreover, it was collaborated with grain refinement of RA, which increased mechanical stability of RA. The grain refinement effect by the TRIP progressed continuously, which increased the stability of RA during plastic deformation in the as-built samples. For this reason, higher stresses were continuously required to transform the remaining RA in the as-built samples.

In contrast, aged-samples hardly require higher stresses to transform the remaining RA, indicating that the stability was almost maintained constantly. This should be because RA grains possess relatively homogeneous composition by aging and the RA grains are suppressed by rigid surrounding phase. The similar grain refinement effect shown in the as-built samples would be applied to the RA grains of the aged samples. However, the boundaries effect generated from newborn martensite within the RA by the TRIP were not as effective as the contributions of pre-existing harder surrounding phase (precipitation-harden martensite),

because transformation was induced at higher stress value than as-built samples. It led to similar phase strains of the RA during TRIP progress in the aged samples (Fig. 5c).

Given that chemical homogeneity affects mechanical stability of RA in as-built and aged samples, it should influence stacking fault energy (SFE) of RA. Thus, stacking fault probability (SFP, P_{sf}) of horizontal samples with a relatively greater RA fraction were taken into consideration [49, 50]. Stacking faults, planar defects, cause a larger hardening in the dense plane FCC{222} than in FCC{111}, which affects difference in hardening of lattice strain. Its probability can be derived by Eq. 4 [51].

$$P_{sf} = \frac{\epsilon^{222} - \epsilon^{111}}{0.05172} \tag{4}$$

Note that the SFP and SFE have an inverse relationship (Supplementary material). The difference in lattice strains between FCC{111} and FCC{222} in the as-built and aged samples was clearly observed in an increase of applied strains (Fig. 8a, b). Both samples had clearly generated SFs that would later grow into TRIP. SFP was determined using the difference in lattice strains and Eq. 4, and it was presented in Fig. 8c as a function of true strain. Although the SFP difference between H-AB and H-A was not great, the SFP of H-A was unquestionably higher than H-AB in the all stage of plastic deformation. It shows that, in contrast to as-built samples, SFs and TRIP in aged samples are easily triggered by deformation. It might be due to the fact that aging treatment changed the chemical composition.

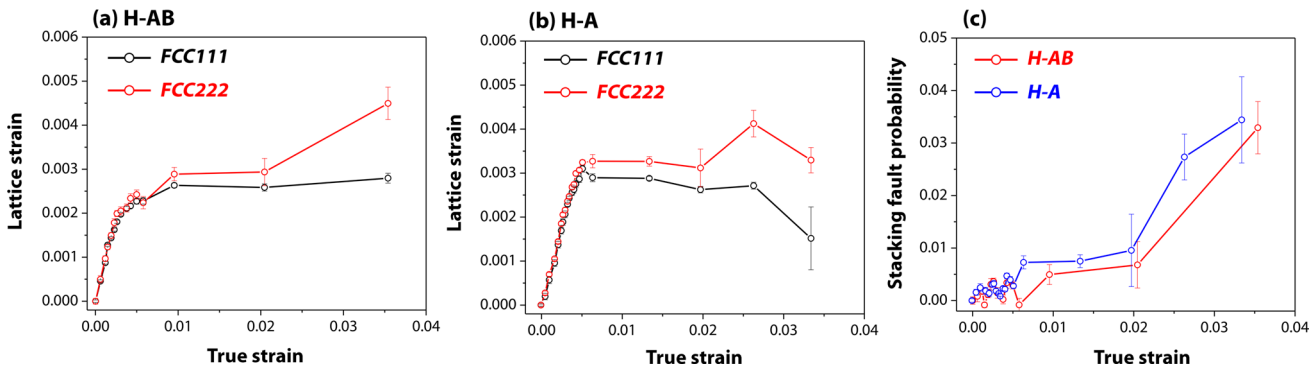

Fig. 8 Lattice strain of FCC{111} (black) and FCC{222} (red) reflection planes in **a** H-AB, **b** H-A, and **c** stacking fault probability of H-AB (red) and H-A (blue) samples as a function of true strain

As a result, aged samples showed higher reduction in relative RA fraction than as-built samples (Fig. 5b).

The RA refinement effect associated with the generation of newborn martensite continuously increased the stability of RA during TRIP progress in the as-built samples, while the RA stability of the aged samples kept constant, revealing that a harder neighbored precipitated-martensite played more important role than the RA refinement. The apparent difference in the shape and size of the RA between the samples at the initial state was hardly discovered in our earlier works [36–38], and the development of the RA texture could also be negligible as aforementioned. The empirical equation using lattice parameters can allow us to compare the effect of concentration of interstitial atoms [52], however, the interpretation is controversial [15]. The largest difference between the as-built and aged samples is based on the hardening of the surrounding martensitic matrix by Cu-precipitation [29, 37]. Therefore, it is suggested that the different resistance to plastic deformation in the neighbored phases principally influenced the stability of RA, resulting in different onset and propagation of TRIP in the as-built and aged samples. In summary, a harder neighboring martensitic matrix delayed the initiation of TRIP in RA of the aged samples under sufficiently higher stress conditions. Subsequently, the activated TRIP at further loading provided a plastic flow and strengthening by newborn martensite.

Austenite retention can reduce aging efficiency, particularly in Cu bearing PH steel due to its higher Cu solubility [29]. In comparison to a counterpart made entirely of martensite, the improvement in YS caused by aging-treatment may be less pronounced in the sample containing RA. While the intrinsic stability was diminished due to the decrease of SFE caused by aging-treatment, the stability of RA was extrinsically improved by the hardened adjacent martensitic phase, successfully increasing the combination of TS and ductility, consequently (Fig. 4c).

It is extrapolated that a similar deformation mechanism can be applied from the fact that the development of the diffraction intensities of the martensite in the current study had good agreement with the previous work [53]. Thus, the deformable potential based on slip could be quantitatively estimated from the intensity evolution of measurable BCT{110} which always increased during plastic deformation in the axial direction. While the vertical samples exhibited a relative intensity of ~ 1.37 at necking, the horizontal samples revealed an intensity of ~ 1.67, which indicates that their deformation textures were more developed in the horizontal samples (Fig. 7). We postulate wrought TRIP steel, manufactured by thermomechanical control process, as criterion counterpart, demonstrating ~ 1.5 in BCC/BCT{110} peak at the necking, to compare evolution of relative intensity of AM samples [54]. In comparison with wrought TRIP steel, vertical and horizontal samples showed lower and higher development of deformation texture. Thus, it is thought that the initial texture imposed by horizontal building strategy was more favorably oriented to develop the deformation texture, which induced a higher magnitude of dislocation glide up to necking, improving uniform elongation of horizontal samples.

5 Conclusions

The horizontally-built strategy imposed more favorable initial texture for plastic deformation, which allowed horizontally-built samples to exhibit enhanced uniform elongation than vertically-built samples. Abrupt TRIP of higher retained austenite fraction during deformation resulted in a higher plastic flow, which led to extended elastic-plastic transition in the horizontally-built sample. Subsequent newborn martensite transformed from retained austenite induced rapid strain hardening, which caused a cross-over in the stress-strain curve and higher tensile strength and ductility.

The aging-treatment decreased the intrinsic stability of RA increasing a SFP, but effectively increased the extrinsic stability delaying the onset of TRIP and strengthening a neighbored martensitic matrix. While RA refinement continuously increased the RA stability during TRIP progress in the as-built samples, the RA stability of the aged samples maintained constant, indicating that a harder neighbored pre-existing precipitated-hardened martensitic matrix played more important role in the aged sample.

Supplementary Information The online version contains supplementary material available at https://doi.org/10.1007/s12540-023-01575-8.

Acknowledgements This work was supported by a National Research Foundation (NRF) grant funded by the Korean government (2021R1A4A1031494, 2020K2A9A2A06070856, 2023R1A2C2007190). The neutron experiments were performed at the BL19 in the Japan Proton Accelerator Research Complex with the proposal 2018A0101. EWH is grateful to the support of the Ministry of Science and Technology (MOST) Programs MOST 110-2224-E-007-001 and MOST 108-2221-E-009-131-MY4. EWH is supported by the Higher Education Sprout Project of the National Yang Ming Chiao Tung University and the Ministry of Education (MOE), Taiwan. EWH very much appreciates the financial support from the Neutron Program of the National Synchrotron Radiation Research Center (NSRRC). HC was supported by the KAERI Institutional program (Project No. 1711139323). SH is grateful for the support of the MEXT Program: Data Creation and Utilization Type Material Research and Development (JPMXP1122684766).

Author Contributions HC Investigation, Formal analysis, Validation, Writing-Original Draft. E-WH Conceptualization, Resources, Validation, Writing-Review & Editing. JJ Validation, Writing-Review & Editing. D-HL Validation, Writing-Review & Editing. SH Validation, Writing-Review & Editing. TK Validation, Data Curation. SYL Conceptualization, Methodology, Validation, Writing-Original Draft, Supervision, Project administration, Funding acquisition.

Data Availability The data that support the findings of this study are available upon request.

Declarations

Conflict of interest The authors declare no conflict of interest

References

1. M. De Meyer, D. Vanderschueren, B. De Coomaim, ISIJ Int. **39**, 813 (1999)
2. B.G. Zhang, X.M. Zhang, H.B. Li, H.T. Liu, Met. Mater. Int. **29**, 607 (2023)
3. X.C. Xiong, B. Chen, M.X. Huang, J.F. Wang, L. Wang, Scr. Mater. **68**, 321 (2013)
4. E. Jimenez-Melero, N.H. van Dijk, L. Zhao, J. Sietsma, S.E. Offerman, J.P. Wright, S. van der Zwaag, Scr. Mater. **56**, 421 (2007)
5. J. Wang, S. Van der Zwaag, Metall. Mater. Trans. A **32**, 1527 (2001)
6. P.J. Jacques, Q. Furnémont, F. Lani, T. Pardoen, F. Delannay, Acta Mater. **55**, 3681 (2007)
7. Y.F. Shen, L.N. Qiu, X. Sun, L. Zuo, P.K. Liaw, D. Raabe, Mater. Sci. Eng. A **636**, 551 (2015)
8. R. Blondé, E. Jimenez-Melero, L. Zhao, J.P. Wright, E. Brück, S. Van Der Zwaag, N.H. Van Dijk, Acta Mater. **60**, 565 (2012)
9. G.K. Tirumalasetty, M.A. Van Huis, C. Kwakernaak, J. Sietsma, W.G. Sloof, H.W. Zandbergen, Acta Mater. **60**, 1311 (2012)
10. C. Song, H. Yu, L. Li, T. Zhou, J. Lu, X. Liu, Mater. Sci. Eng. A **670**, 326 (2016)
11. W. Choo, M. Ebrahimian, K. Choi, J.H. Kim, Met. Mater. Int. **29**, 1750 (2023)
12. C. Garcia-Cabezon, M.A. Castro-Sastre, A.I. Fernandez-Abia, M.L. Rodriguez-Mendez, F. Martin-Pedrosa, Met. Mater. Int. **28**, 2652 (2022)
13. J. Tiwari, B.K. Mahanta, H. Krishnaswamy, S. Devadula, M. Amirthalingam, Met. Mater. Int. **29**, 2287 (2023)
14. P. Bajaj, A. Hariharan, A. Kini, P. Kürnsteiner, D. Raabe, E.A. Jägle, Mater. Sci. Eng. A **772**, 138633 (2020)
15. H. Chae, E.-W. Huang, W. Woo, S.H. Kang, J. Jain, K. An, S.Y. Lee, J. Alloys Compd. **857**, 157555 (2020)
16. E.-W. Huang, S.Y. Lee, J. Jain, Y. Tong, K. An, N.-T. Tsou, T.-N. Lam, D. Yu, H. Chae, S.-W. Chen, S.-M. Chen, H.-S. Chou, Intermetallics **109**, 60 (2019)
17. S.D. Meredith, J.S. Zuback, J.S. Keist, T.A. Palmer, Mater. Sci. Eng. A **738**, 44 (2018)
18. L. Murr, E. Martinez, S. Gaytan, D. Ramirez, B. MacHado, P. Shindo, J. Martinez, F. Medina, J. Wooten, D. Ciscel, U. Ackelid, R. Wicker, Metall. Mater. Trans. A **42**, 3491 (2011)
19. S. Primig, G. Stechauner, E. Kozeschnik, Steel Res. Int. **88**, 1 (2017)
20. L. Wang, C. Dong, D. Kong, C. Man, J. Liang, C. Wang, K. Xiao, X. Li, Steel Res. Int. **91**, 1900447 (2020)
21. X.D. Nong, X.L. Zhou, Y.D. Wang, L. Yu, J.H. Li, Mater. Sci. Eng. A **821**, 141587 (2021)
22. X.D. Nong, X.L. Zhou, Mater. Charact. **174**, 111012 (2021)
23. S. Pal, H.R. Tiyyagura, I. Drstvenšek, C.S. Kumar, Procedia Eng. **149**, 359 (2016)
24. H.K. Rafi, T.L. Starr, B.E. Stucker, Int. J. Adv. Manuf. Technol. **69**, 1299 (2013)
25. B.H.R. Habibi, Mater. Sci. Eng. A **338**, 142 (2002)
26. X.D. Nong, X.L. Zhou, J.H. Li, Y.D. Wang, Y.F. Zhao, M. Brochu, Scr. Mater. **178**, 7 (2020)
27. H.K. Rafi, D. Pal, N. Patil, T.L. Starr, B.E. Stucker, J. Mater. Eng. Perform. **23**, 4421 (2014)
28. H.J. Rack, D. Kalish, Metall. Mater. Trans. B **5**, 1595 (1974)
29. Z. Wang, H. Li, Q. Shen, W. Liu, Z. Wang, Acta Mater. **156**, 158 (2018)
30. L. Jiang, C. Chen, M. Zhang, Met. Mater. Int. **29**, 141 (2023)
31. A. Kudzal, B. McWilliams, C. Hofmeister, F. Kellogg, J. Yu, J. Taggart-Scarff, J. Liang, Mater. Des. **133**, 205 (2017)
32. M. Mahmoudi, A. Elwany, A. Yadollahi, S.M. Thompson, L. Bian, N. Shamsaei, Rapid. Prototyp. J. **23**, 280 (2017)
33. A. Caballero, J. Ding, S. Ganguly, S. Williams, J. Mater. Process. Technol. **268**, 54 (2019)
34. E.A. Lass, M.R. Stoudt, M.E. Williams, Metall. Mater. Trans. A **50**, 1619 (2019)
35. X. Zhao, S. Dong, S. Yan, X. Liu, Y. Liu, D. Xia, Y. Lv, P. He, B. Xu, H. Han, Mater. Sci. Eng. A **771**, 138557 (2020)
36. H. Chae, E.-W. Huang, J. Jain, H. Wang, W. Woo, S.W. Chen, S. Harjo, T. Kawasaki, S.Y. Lee, Mater. Sci. Eng. A **762**, 138065 (2019)
37. H. Chae, E.-W. Huang, M.Y. Luo, E. Shin, C. Do, S.-K. Hong, W. Woo, S.Y. Lee, E.-W. Huang, E. Shin, C. Do, S.-K. Hong, W. Woo, S.Y. Lee, Mater. Charact. **184**, 111645 (2022)
38. J.-R. Lee, M.-S. Lee, H. Chae, S.Y. Lee, T. Na, W.-S. Kim, T.-S. Jun, Mater. Charact. **167**, 110468 (2020)
39. A. Bohlen, H. Freiße, M. Hunkel, F. Vollertsen, Procedia CIRP **74**, 192 (2018)
40. L. Couturier, F. De Geuser, M. Descoins, A. Deschamps, Mater. Des. **107**, 416 (2016)
41. J. Gao, S. Jiang, H. Zhang, Y. Huang, D. Guan, Y. Xu, S. Guan, L.A. Bendersky, A.V. Davydov, Y. Wu, H. Zhu, Y. Wang, Z. Lu, W.M. Rainforth, Nature **590**, 262 (2021)
42. Z. Li, K.G. Pradeep, Y. Deng, D. Raabe, C.C. Tasan, Nature **534**, 227 (2016)
43. EOS Material Data Sheet, https://Www.Eos.Info/En/Additive-Manufacturing/3d-Printing-Metal/Dmls-Metal-Materials/Stainless-Steel
44. CLIFFS Material Data Sheet. https://Www.Clevelandcliffs.Com/Products
45. S. Harjo, T. Kawasaki, N. Tsuchida, S. Morooka, W. Gong, ISIJ Int. **61**, 648 (2020)
46. J. Quinta da Fonseca, E.C. Oliver, P.S. Bate, P.J. Withers, Mater. Sci. Eng. A **437**, 26 (2006)
47. M. Uchikoshi, K. Matsuda, Y. Onuki, K. Shinoda, S. Suzuki, ISIJ Int. **62**, 970 (2022)
48. B. Clausen, T. Lorentzen, M.A.M. Bourke, M.R. Daymond, Mater. Sci. Eng. A **259**, 17 (1999)
49. W. Woo, Y.S. Kim, H.B. Chae, S.Y. Lee, J.S. Jeong, C.M. Lee, J.W. Won, Y.S. Na, T. Kawasaki, S. Harjo, K. An, Acta Mater. **246**, 118699 (2023)
50. Y.S. Kim, H. Chae, W. Woo, D.K. Kim, D.H. Lee, S. Harjo, T. Kawasaki, S.Y. Lee, Mater. Sci. Eng. A **828**, 142059 (2021)
51. R.P.I. Adler, H.M. Otte, C.N.J. Wagner, Metall. Trans. **1**, 2375 (1970)
52. Y. Tomota, H. Tokuda, Y. Adachi, M. Wakita, N. Minakawa, A. Moriai, Y. Morii, Acta Mater. **52**, 5737 (2004)
53. H. Choo, M.R. Koehler, L.P. White, Y. Ren, D. Morin, E. Garlea, Mater. Sci. Eng. A **791**, 139637 (2020)
54. O. Muránsky, P. Šittner, J. Zrník, E.C. Oliver, Acta Mater. **56**, 3367 (2008)